Structure and laminar flame speed of an ammonia/methane/air premixed flame under varying pressure and equivalence ratio

Rocha, Rodolfo C.; Zhong, Shenghui; Xu, Leilei; Bai, Xue Song; Costa, Maìrio; Cai, Xiao; Kim, Haisol; Brackmann, Christian; Li, Zhongshan; Aldeìn, Marcus

Published in:
Energy and Fuels

DOI:
10.1021/acs.energyfuels.0c03520

2021

Document Version:
Publisher's PDF, also known as Version of record

energy&fuels

pubs.acs.org/EF

Article

Structure and Laminar Flame Speed of an Ammonia/Methane/Air Premixed Flame under Varying Pressure and Equivalence Ratio

Rodolfo C. Rocha, Shenghui Zhong, Leilei Xu, Xue-Song Bai,* Mário Costa, Xiao Cai, Haisol Kim, Christian Brackmann,* Zhongshan Li, and Marcus Aldén

Cite This: *Energy Fuels* 2021, 35, 7179–7192

Read Online

ACCESS | Metrics & More | Article Recommendations

ABSTRACT: This paper presents a joint experimental and numerical study on premixed laminar ammonia/methane/air flames, aiming to characterize the flame structures and NO formation and determine the laminar flame speed under different pressure, equivalence ratio, and ammonia fraction in the fuel. The experiments were carried out in a lab-scale pressurized vessel with a Bunsen burner installed with a concentric co-flow of air. Measurements of NH and NO distributions in the flames were made using planar laser-induced fluorescence. A novel method was presented for determination of the laminar flame speed from Bunsen-burner flame measurements, which takes into account the non-uniform flow in the unburned mixture and local flame stretch. NH profiles were chosen as flame front markers. Direct numerical simulation of the flames and one-dimensional chemical kinetic modeling were performed to enhance the understanding of flame structures and evaluate three chemical kinetic mechanisms recently reported in the literature. The stoichiometric and fuel-rich flames exhibit a dual-flame structure, with an inner premixed flame and an outer diffusion flame. The two flames interact, which affects the NO emissions. The impact of the diffusion flame on the laminar flame speed of the inner premixed flame is however minor. At elevated pressures or higher ammonia/methane ratios, the emission of NO is suppressed as a result of the reduced radical mass fraction and promoted NO reduction reactions. It is found that the laminar flame speed measured in the present experiments can be captured by the investigated mechanisms, but quantitative predictions of the NO distribution require further model development.

INTRODUCTION

The growing demand of energy and the urgent need of reducing the emission of greenhouse gases are the main drivers of the development of disruptive technologies for clean power production. For land-based applications, solar-, wind-, and biomass-based energy production systems have been developed extensively.[1] For other applications, such as maritime transportation, vehicles, and power generation in places depleted of natural resources, other solutions must be implemented, and as a result of the requirements in terms of energy density and reliability, the use of combustion systems running carbon-neutral or carbon-free fuels has been suggested.[2−5]

Ammonia (NH_3) is considered a possible candidate fuel in the future carbon-free energy system.[2,3] It is cost-effective to produce, being mainly formed by the traditional Haber−Bosch process, using hydrogen (H_2) as a source. Despite generating carbon dioxide (CO_2) with this method, especially when hydrogen comes from natural gas reforming, a wide variety of available generation processes, including some that are considered "green", using renewable sources, or "blue", which include carbon capture, are capable of mitigating these emissions. Ammonia is also safe and simple to transport and store, especially when compared to other carbon-free fuels, such as hydrogen, as a result of its low reactivity and low pressure of condensation, which allows it to be stored in liquid form at ambient temperature and pressure as low as 10 bar. Moreover, as a consequence of its widespread use in the fertilizer industry, a mature network of production, handling, transportation, and storage is already established worldwide.[2,3]

In combustion systems, however, the oxidation of ammonia presents a series of challenges as a result of its unique characteristics. First, as a result of its low reactivity, pure ammonia shows low laminar burning velocities, long ignition delay times, and problematic flame stabilization. Second, it generates high levels of nitrogen oxides, mostly by the fuel NO route, as well as harmful unburned ammonia emissions in real combustion systems, thus requiring new or adapted methods of firing or post-flame catalysis systems to be applied safely. Ammonia has been tested in several real-life applications over the years, and more recently, the interest in decarbonation led to several applied studies. For internal combustion engines, works on both spark-ignition (SI)[6−10] and compression-ignition (CI)[11−13] systems were reported, making use of some advantageous characteristics of ammonia, such as its high energy density in liquid form. Commercially, a dual-fuel ammonia two-stroke marine combustion engine is already in

Special Issue: In Memory of Mario Costa

Received: October 20, 2020
Revised: January 8, 2021
Published: January 22, 2021

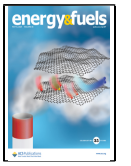

development.[14] For SI engines, the high octane number of NH_3 makes it an interesting option, while its characteristics of low reactivity can be mitigated by its mixing with[6,8] or partial cracking into hydrogen,[9,15] optimizing its performance. Mørch et al.[6] found that, in a SI engine, fuel mixtures with 10%$_{vol}$ H_2 present better performance than pure NH_3 firing or with higher concentrations of H_2, also noticing lower NO_x emissions for fuel/air equivalence ratios from 1.1 to 1.4. More recently, Lhuillier et al.[10] studied the heat-release profiles when blending ammonia with methane (CH_4) and hydrogen in a single-cylinder SI engine. Reiter and Kong,[11] on the other hand, were some of the first to explore ammonia in CI engines, who demonstrated the feasibility of diesel−ammonia blends, despite the difficulty in igniting the mixtures, also determining that, for up to 60% of ammonia in energy load, NO_x emissions did not increase significantly; it was also detected, however, that unburned hydrocarbon emissions increased. Similar conclusions were drawn by Ryu et al.,[12] who tested ammonia/dimethyl ether (DME) mixtures. It is worth noticing that most works on combustion engines found in the literature use dual-fuel approaches. Pure ammonia firing, as a result of its difficulty of ignition, low flame speed, and low reactivity, was seldom reported.[7,13] In this context, novel methods are needed to improve the flame speed.[7]

Another combustion application being considered suitable for ammonia is that of stationary gas turbines. Kurata et al.[16] reported a study of NH_3/air and NH_3/CH_4/air premixed flames in a micro gas turbine, showing that stable pure ammonia flames are possible in conventional systems. Blending ammonia with methane was shown to increase combustion efficiency and flame speed; however, NO_x emissions increase with the molar ratio of methane in the ammonia/methane mixture, up to a volume fraction of 0.4 of methane. Hayakawa et al.[17] studied premixed flames of pure ammonia in a swirl burner, showing that NO_x emissions increase with fuel/air equivalence ratio up to 0.9 and sharply decrease afterward. For fuel-rich flames, a drastic increase of unburned ammonia emissions as well as hydrogen were detected in the flue gas. In subsequent studies,[18,19] the same group explored staged combustion systems, in rich−lean configurations, to increase the combustion efficiency and reduce global NO_x and NH_3 emissions. Using an optimal configuration, the emissions for NO_x were shown to be as low as 42 ppmv, with negligible emissions of NH_3. They also found that higher pressures help mitigate NO_x formation. Valera-Medina et al.[20] also explored NH_3/CH_4 and NH_3/H_2 fuel mixtures in a swirl burner, corroborating the findings of Hayakawa et al.[17] in terms of the effect of equivalence ratio, detecting high carbon monoxide (CO) emissions for NH_3/CH_4/air flames for equivalence ratios higher than 0.9. The same group also further explored fuel-rich[21] and fuel-lean[22] premixed NH_3/H_2/air flames in the same burner as well as staging, high pressure, and humidification as means of controlling NO_x emissions.[23]

Recent works in the field include that of Mario Costa's group,[24] who developed a swirl- and bluff-body stabilized burner for partially premixed NH_3/H_2/air combustion, demonstrating the flame stability for a range of equivalence ratios and fuel compositions, and the possibility of NO_x mitigation by selective non-catalytic reduction (SNCR) using stratified ammonia in the combustor. The same group also explored the advantages of using combustor staging or moderate or intense low-oxygen dilution (MILD) combustion in gas turbines to drastically reduce NO_x emissions of ammonia flames.[25]

Despite all of the developments in the usage of ammonia in applied systems, the fundamentals of ammonia combustion are still to be explored. Historically, the chemical kinetic mechanism of Miller and Bowman[26] was one of the first to describe nitrogen chemistry in flames. Skreiberg et al.[27] improved the mechanism of Miller and Bowman[26] by including SNCR reactions for the NO_x reduction pathways. Dagaut et al.[28] studied the hydrogen cyanide chemistry in combustion, by adding reactions related to nitrogen−carbon interaction to the mechanism of Skreiberg et al.[27] The mechanism allowed for a better understanding of the prompt and fuel NO formation processes. Konnov[29] studied the NCN pathways, incorporating prompt NO reactions into a full mechanism for small hydrocarbons.

Further enhancements to these mechanisms were made by other authors to match experimental data for different conditions.[30−34] Among these, it is worth mentioning the mechanism of Tian et al.,[30] which contains 84 species and 703 reactions. The mechanism was based on the work of Skreiberg et al.[27] and findings from other authors.[30] Mendiara and Glarborg[31] further developed the mechanism of Tian et al.[30] by including ammonia chemistry in oxy-fuel combustion, obtaining a mechanism with 97 species and 779 reactions. More recently, Glarborg et al.[35] reported a full mechanism for nitrogen chemistry, including sub-mechanisms for ammonia combustion, SNCR processes, and related chemistry, containing 151 species and 1397 reactions. Another recent mechanism is that of Li et al.,[36] which was developed on the basis of Konnov's mechanism[29] by including chemistry optimized for ammonia combustion with both methane and hydrogen enrichment. This mechanism contains 128 species and 957 reactions in its full form; the mechanism was validated against experimental data on the laminar flame speed, ignition delay times, and species profiles for a number of conditions.

Rocha et al.[37] evaluated the performance of 10 different chemical kinetic mechanisms containing nitrogen chemistry by comparing to experimental data for the laminar flame speed and ignition delay times for NH_3/air and NH_3/H_2/air flames. While the mechanisms yielded very scattered results, three were shown to perform better in ammonia flame simulations: the mechanism of Mathieu and Petersen,[38] containing 55 species and 278 reactions, the mechanism of Otomo et al.,[39] containing 32 species and 213 reactions, and the mechanism of Okafor et al.,[40] containing 59 species and 356 reactions. The Okafor mechanism was developed on the basis of the GRI-Mech 3.0 mechanism[41] for hydrocarbon oxidation and the mechanism of Tian et al.[30] for nitrogen chemistry and validated for laminar burning velocities of NH_3/CH_4/air flames. Rocha et al.[25] also evaluated some other mechanisms for NO formation in ammonia/air flames, comparing to experimental data from Brackmann et al.,[42] showing that the mechanism of Mendiara and Glarborg[31] and the mechanism of Okafor et al.[40] performed better in NO prediction.

Several studies have shown that NO emission can be promoted when co-firing ammonia with other fuels.[16,43] Ramos et al.[43] studied NO_x emissions in premixed laminar NH_3/CH_4/air flames at ambient conditions, showing that the NO_x emissions peak for volume fractions of 0.5 of CH_4 in the fuel. Numerical studies by the authors predicted trends similar to the experimental ones, despite overpredicting the emissions. Sensitivity analysis indicated that NO formation is sensitive to

https://dx.doi.org/10.1021/acs.energyfuels.0c03520
Energy Fuels 2021, 35, 7179−7192

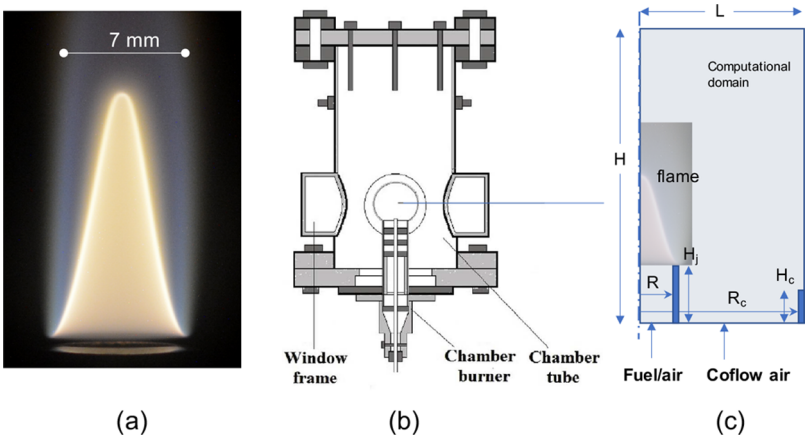

Figure 1. (a) Picture of an NH_3/CH_4/air premixed flame under an NH_3/CH_4 molar ratio of 0.60/0.40, pressure of 3 bar, and equivalence ratio of 1.2 and (b) schematic illustration of the pressurized vessel and the burner, (c) along with the computational domain of a size of H = 59 mm and L = 19.5 mm. Burner inner radius, R = 3.5 mm; co-flow tube inner radius, R_c = 17.5 mm; burner wall thickness = 1.5 mm; burner length, H_j = 14 mm; and co-flow tube length, H_c = 10 mm.

H_2/O_2 oxidation reactions through the HNO formation and oxidation routes. NO formation is promoted by oxygen excess and methane enrichment while being mitigated by higher concentrations of $N/NH/NH_2$ radicals, which react with NO. These NO reduction reactions are enhanced by oxygen depletion. The authors also indicated that competition for oxygen may promote CO emissions under some conditions. Rocha et al.[44] measured NO_x and unburned NH_3 emissions in NH_3/H_2/air and NH_3/CH_4/air flames in a porous media burner, which attested to the effects of the reaction paths indicated in the previous work.[43]

Laser-based methods are highly valuable for non-intrusive measurements in combustion to provide data for model validation and have also been applied in studies of ammonia combustion. One early example is the investigations by Chou et al.,[45] who carried out laser-induced fluorescence (LIF) measurements of nitric oxide (NO) in NH_3-doped CH_4 flames with air as an oxidizer. Later studies with LIF measurements of NO in such flames have been presented by Li et al.[46] and Brackmann et al.[47] Moreover, profiles of NH, OH, and NO have been measured in flames burning neat NH_3[42,48] or NH_3 co-firing with H_2.[49]

These previous laser diagnostic studies were carried out under low-pressure[48,49] or atmospheric[42,45,47] conditions. In this study, we extend investigations to elevated pressures to obtain data for further development and validation of ammonia chemistry. Experimental data include laminar flame speed and species profiles for characterization of reaction-zone structures and are used to evaluate the most recent chemical kinetic mechanisms for ammonia flames.[35,36,40] A pressurized constant-pressure combustion vessel with a Bunsen burner installed in a co-flow air environment is employed for the experiments. Because the flames are of a complex structure involving multiple flame modes and flame stretch, a direct numerical simulation (DNS) of the flame is performed employing the Okafor mechanism[40] as a result of its relatively low computational demand. On the basis of the DNS results, a novel method of determining the laminar flame speed from conical Bunsen-type flames is developed and validated. In the experiments, planar LIF imaging of NH and NO are performed under different equivalence ratio, pressure, and ammonia/methane ratio conditions, to investigate the NO_x promotion/mitigation. To the best knowledge of the authors, no other works of this kind have been reported in the literature. This thus increases the level of complexity with the goal to assess possibilities for modeling NH_3 combustion under more realistic conditions, which is a necessary step toward introducing NH_3 as a component in a future sustainable energy supply.

EXPERIMENTAL METHODS

Laser-induced fluorescence measurements were carried out to study the structures of ammonia/methane/air premixed flames stabilized on a Bunsen burner installed in a pressurized constant-pressure vessel. Investigations were carried out under different molar fractions of NH_3 in the NH_3 and CH_4 mixture (0.2−0.8), equivalence ratios (0.8−1.2), and pressures (1−3 bar). Fuel/air equivalence ratios (ϕ) are calculated considering full conversion of ammonia into H_2O and N_2 as well as full conversion of CH_4 into H_2O and CO_2 (see formulation by Rocha et al.[44]). In this section, a brief description of the experimental rig is presented, while more details about the rig can be found in refs 50 and 51.

Experimental Rig and Apparatus. Figure 1 shows the experimental rig and a picture of a premixed NH_3/CH_4/air flame. The pressurized vessel is made of stainless steel; it has a cylindrical shape with an inner diameter of 254.5 mm and an inner height of 500 mm. The rig can operate at a maximum pressure of 36 bar and a maximum ambient temperature of 220 °C. Optical access to the flame is available through four viewports positioned at angles of 0°, 90°, 180°, and 270°. The pressure inside the vessel is kept constant by regulating the exiting gas flow rate using back-pressure regulators. The experiments were conducted at constant pressures, with a fluctuation of less than 1%.

The burner is composed of a central jet with an inner radius (R) of 3.5 mm and a coaxial annular tube with an inner radius (R_c) of 17.5 mm. The fuel/air mixture was supplied through the center jet, whereas co-flow air was supplied through the annular tube (cf. Figure 1c). The flow rates of the fuel/air mixture were regulated by mass-flow controllers (MFCs, Brooks and Bronkhorst). The flame was monitored continuously by a digital camera (D7100, Nikon) equipped with an f = 200 mm AF Micro Nikkor lens. Figure 1a shows a photo of the flame at an equivalence ratio of 1.2, pressure of 3 bar, and NH_3/CH_4 molar ratio of 0.60/0.40. Bright yellow chemiluminiescence from NH_2 radicals is observed in a thin zone, which indicates the position of a premixed flame front. The yellow region is surrounded by a blue luminous layer of a diffusion flame that burns CO and H_2 generated at the premixed flame front.

Laser Diagnostics. Planar laser-induced fluorescence (PLIF) imaging of the NH radical and nitric oxide (NO) was made in the

https://dx.doi.org/10.1021/acs.energyfuels.0c03520
Energy Fuels 2021, 35, 7179−7192

investigated flames. Measurements were made using an Nd:YAG laser (Quanta Ray Pro 200, Spectra Physics) of 20 Hz repetition rate that was pumping a dye laser (Sirah) operated on dye LDS698. For measurements of NH, the dye laser was tuned to wavelength 672 nm and frequency-doubled to 336 nm for excitation of NH in the (0−0) band of the $A^3\Pi-X^3\Sigma^-$ transition. Measurements of NO were made with the laser tuned to wavelength 676.5 nm, which was converted to 225.5 nm by frequency-tripling (doubling combined with mixing) for excitation of the $Q_2(26.5)$ transition in the (0−0) band of the $A^2\Sigma^+-X^2\Pi$ transition. Typical pulse energies for excitation of NH and NO were 10 and 0.5 mJ/pulse, respectively, and the laser linewidth was measured using an etalon to be 0.3 cm^{-1} (corresponding to 7 GHz). The ultraviolet laser beams were shaped using a concave cylindrical lens (f = −50 mm) combined with a spherical lens (f = +300 mm) resulting in a focused vertical laser sheet crossing above the burner orifice through the center of the flames. Fluorescence was imaged perpendicularly to the laser sheet with an intensified charge-coupled device (CCD) camera (P-IMAX2, Princeton Instruments) equipped with an f = +100 mm, $f/\#$ = 2 objective (B. Halle), and extension tubes. For measurements of NO, a long-pass filter (WG225, Schott) was used to suppress scattering and straylight at the laser wavelength, whereas measurements of NH were made resonantly in the (0−0) band without filter. For the latter case, the PLIF signal was sufficiently strong to dominate over undesired backgrounds and provide high-contrast images of NH present in the flame front (the brightest zone in Figure 1c).

The PLIF signal of NO was converted into mole fraction according to the theory for LIF outlined by Eckbreth[52] and based on eq 1

$$N_i = 4\pi c\frac{A+Q}{A}\frac{S_{\mathrm{LIF}}}{BI_\nu\Omega l\varepsilon} \tag{1}$$

where N_i is a number density corresponding to the fraction of NO molecules that populate the lower energy level excited by the laser. Other quantities in eq 1 are the speed of light c, the coefficient of spontaneous emission A, the collisional quenching rate Q, the LIF signal S_{LIF}, the absorption coefficient B, the laser spectral irradiance I_ν, the solid angle of the LIF signal collection Ω, the measurement volume length l and the detector efficiency ε. Coefficients A and B of spontaneous emission and absorption for NO, respectively, were obtained from the LIFBASE software.[53] Data on collisional quenching of NO were obtained from quenching cross-sections presented by Settersten et al.[54] The cross sections were combined with major species concentrations retrieved from DNS results to calculate the total collisional quenching rate, Q, in eq 1. The spectral irradiance factor, I_ν, was calculated from the laser pulse energy and also included the overlap between the laser spectral profile and the shape of the NO $Q_2(26.5)$ absorption line, for which parameters were obtained from ref 55. A pressure-induced shift in the position of the NO $Q_2(26.5)$ absorption line was also included in the evaluation.[55]

For elastic scattering of laser light by atoms and molecules, i.e., Rayleigh scattering, the number of scattered photons is proportional to the number of incident laser photons, a scattering cross-section, and the quantities Ω, l, and ε. A Rayleigh scattering measurement in ambient air thus provided the product of these quantities and allowed for calibration of the light collection geometry and detector response. The total number density of NO molecules is calculated from N_i by division with a population factor from the temperature-dependent Boltzmann distribution, which was also retrieved from LIFBASE.[53] The total number density retrieved can then be converted into mole fraction by means of the ideal gas law.

While the spectroscopic quantities A and B for NO are known with high accuracy, the other quantities in eq 1 are associated with experimental uncertainties. The uncertainty in instrument readings of laser energy was estimated to be 7% and contributes to the corresponding uncertainty of the laser spectral irradiance I_ν. Moreover, the same uncertainty is included in the Rayleigh scattering measurements made to determine the product of factors Ω, l, and ε. In addition, Rayleigh scattering measurements are sensitive to the false-positive signal from straylight. In the present experimental setup, scattering should ideally only be detected for vertical polarization of the laser. However, a comparison between scattering measurements of air inside the high-pressure vessel for orthogonal laser polarizations indicates that up to 20% of the detected signal could be due to straylight, thus introducing a corresponding experimental uncertainty for the scattering measurements. The laser spectral irradiance includes the overlap between the laser spectral profile and the NO absorption line; i.e., it depends upon the laser wavelength as well as the linewidth. The laser wavelength was tuned to the NO $Q_2(26.5)$ absorption line, and the wavelength was monitored by a wavemeter with an accuracy of 0.001 nm. A potential drift in wavelength within this accuracy, i.e., of 0.0005 nm, results in an additional uncertainty for the spectral irradiance factor of 20%. The evaluation showed less sensitivity to the laser spectral width, for which re-evaluation with a value only half of the measured value introduced a relative change in the results by 2%. Uncertainties in the temperature also have an impact on evaluated results through the temperature-dependent Boltzmann population factor and the collisional quenching rate, Q. For a temperature uncertainty of 100 K, both of these quantities introduce an uncertainty of 2%. The uncertainty of the signal, S_{LIF}, is associated with background subtraction errors and the reproducibility of the measurements. For the background, an estimated possible error of 10% resulted in a relative change in evaluated mole fractions by 4%. Repeated measurements for the atmospheric case showed a spread in post-flame NO mole fractions by 7%. The total experimental uncertainty was calculated as the root mean square of the individual uncertainties discussed above and was determined to 31%.

Measurement of the Laminar Flame Speed. Assuming that the flow velocity in front of the flame is uniform with a constant axial velocity of U_{jet} and a radial velocity of zero, and that the local displacement speed is the laminar flame speed of the unstretched flame (S_{L}), it can be shown that the flame front satisfies the following analytical expression:

$$x = f(r) = (R-r)(L_{\mathrm{f}}/R) = (R-r)(U_{\mathrm{jet}}{}^2/S_{\mathrm{L}}{}^2 - 1)^{1/2} \tag{2}$$

where x and r are the axial and radial coordinates, respectively, R is the radius of the jet, and L_{f} is the height of the flame. As seen from this expression, the flame is of a conical shape. Equation 2 can be rewritten as

$$S_{\mathrm{L}} = U_{\mathrm{jet}}(R^2/(R^2 + L_{\mathrm{f}}{}^2))^{1/2} = U_{\mathrm{jet}}\sin(\alpha) \tag{3}$$

where α is the half-cone angle of the conical shape flame. Equation 3 offers a way of determining the laminar flame speed from measurement of the flame height or half-cone angle.[51,56−58] This method is hereafter referred to as the flame cone-angle method.

As shown in the Results and Discussion, the fuel/air flow stream remains that of the fully developed pipe flow profile in front of the premixed flame front (the radial velocity component is negligible compared to the axial velocity). Assuming that the axial velocity follows that of a fully developed pipe flow (cf. eq 10), and the local displacement velocity (S_{d}) follows the theory of a stretched flame,[59,60] i.e.

$$S_{\mathrm{d}} = S_{\mathrm{L}} - \mathcal{L}\mathbb{K} \tag{4}$$

it can be shown that the flame front [$x = f(r)$] satisfies the following equation:

$$U(r) = (S_{\mathrm{L}} - \mathcal{L}\mathbb{K})(1 + (f'(r))^2))^{1/2} \tag{5}$$

where $f'(r)$ is the derivative of $f(r)$ and $\mathbb{K}$ is the flame stretch rate

$$\mathbb{K} = S_{\mathrm{L}}\kappa + K_{\mathrm{s}} \tag{6}$$

with κ being the curvature of the flame front

$$\kappa = \frac{\partial}{\partial r}\left(\frac{f'(r)}{(1+(f'(r))^2)^{1/2}}\right) \tag{7}$$

and K_{s} being the strain rate

https://dx.doi.org/10.1021/acs.energyfuels.0c03520
Energy Fuels 2021, 35, 7179−7192

Table 1. Experimental and Computational Cases[a]

case	p_0 (bar)	X_{NH_3}	ϕ	U_{jet} (m/s)	$\dot{m}$ ($\times 10^5$, kg/s)	Re	S_L (cm/s)	L_f (mm)	$\mathcal{L}_{DNS}$ (mm)	$\mathcal{L}_{exp}$ (mm)
1	1	0.2	1.2	1.94	5.85	926	43.2	15.7	0.13	0.176
2	2	0.2	1.2	1.54	9.18	1453	33.3	17.0	0.095	0.083
3	3	0.2	1.2	1.26	11.24	1779	27.9	16.6	0.079	0.032
4	3	0.4	1.2	0.97	8.65	1379	23.6	16.8	0.075	0.081
5	3	0.6	1.2	0.74	6.49	1045	19.3	16.5	0.078	0.079
6	3	0.8	1.2	0.55	4.77	778	16.4	16.4	0.077	0.100
7	3	0.2	0.8	1.1	10.01	1563	26.6	15.9	0.069	0.052
8	1	0.2	1	1.94	5.90	928	51.8	16.1	0.116	0.122
9	2	0.2	1	1.81	10.86	1708	41.6	17.0	0.083	0.077
10	3	0.2	1	1.52	13.74	2162	35.7	16.6	0.072	0.063

[a] U_{jet} is the bulk velocity of inner jet flow; p_0 is the combustor pressure; ϕ is the equivalence ratio; X_{NH_3} is the molar ratio of NH_3 in the NH_3/CH_4 mixture; $\dot{m}$ is the mass flow rate; Re is the Reynolds number based on the bulk flow velocity and burner diameter; S_L is the laminar flame speed from 1D simulation using the Okafor mechanism;[40] L_f is the flame height from experiments; and $\mathcal{L}$ is the Markstein length determined from the DNS results. The co-flow velocity, $U_{co\text{-}flow}$, is about 0.25 m/s, and T_u, the temperature of the fuel/air stream, is kept at 423 K for all cases.

$$K_s = (8rU_{jet}/R^2)\frac{f'(r)}{1 + (f'(r))^2} \tag{8}$$

Equation 5 can be solved numerically given that all flow and flame parameters are known, with S_L being the eigenvalue of the problem. This provides a more accurate method for measuring S_L from the present Bunsen-burner configuration. For a given set of bulk flow velocity U_{jet}, flame height L_f, and Marktein length $\mathcal{L}$, the eigenvalue S_L is obtained by enforcing eq 5 to satisfy the following boundary conditions:

$$f(0) = L_f, \quad f'(0) = 0, \quad f(R) = 0 \tag{9}$$

The uncertainties of the laminar flame speed determined using the above methods will be discussed in the Results and Discussion.

NUMERICAL METHOD AND COMPUTATIONAL SETUP

The governing equations considered in the numerical simulations are the Navier−Stokes equations, the continuity equation, and the transport equations for species mass fractions and enthalpy. The mixture is assumed to follow the ideal gas law. A detailed chemical kinetic mechanism for methane and ammonia, developed by Okafor et al.,[40] was employed in the simulations. The mechanism, as discussed in the Introduction, was developed for mixtures of ammonia and methane. The mechanism was among those that yielded the best prediction of the laminar flame speed against experimental data for a range of equivalence ratios.[37] The mechanism was also among those that best predicted NO formation.[25] The one-dimensional simulations included the mechanisms of Glarborg et al.[35] and Li et al.[36] as well. These three mechanisms represent some of the latest and most comprehensive mechanisms developed for ammonia combustion.

Numerical Solvers. The governing equations are solved numerically using two software, OpenFOAM[61] for the two-dimensional (2D) DNS cases and the Cantera package[62] for one-dimensional (1D) freely propagating flames. In OpenFOAM's original solver, rhoReactingBuoyantFoam, the original transport equations for the species mass fractions and enthalpy were based on two assumptions: a Schmidt number of unity and a Lewis number of unity. This solver also includes corrections for buoyancy. The dynamic viscosity was calculated using the Sutherland equation.[63] Because the original solver was developed mainly for turbulent combustion, for which the molecular preferential diffusion is considered negligible in comparison to the turbulent diffusion, these two assumptions can be regarded as acceptable. However, they are not suitable for the present laminar-flame simulations. To accurately describe the reaction−diffusion process, the mixture-averaged transport model identical to that used in ref 64 was implemented in the current solver. The detailed transport properties for each species were calculated using a third-order logarithm polynomial fitting method.[64] This solver has been successfully applied in our previous study of laminar premixed *n*-heptane/air flames in a low-temperature ignition regime,[65] a spherical laminar premixed flame with intrinsic flame instability,[66] and turbulent flame propagation and ignition.[67,68] A finite-volume method with a linear scheme (second order) was adopted for the space discretization, and a first-order scheme was used for the time integration. Because the flame is steady, a first-order time integration scheme is preferred as a result of its numerical stability. The pressure-implicit-with-splitting-of-operator (PISO) algorithm with four inner correction loops was employed to solve the system of discretized equations.

Case Setup and Boundary Conditions. Because the premixed flame is axisymmetric, a 2D axisymmetric computational domain was specified. The domain is of a wedge shape with a small angle (1°), discretized using one mesh cell in the azimuthal direction. Figure 1c shows the computational domain. The domain was selected such that the far field boundary of the domain is sufficiently far away from the flame where the local mixture is pure air and the local flow velocity is low. A uniform rectangular grid with a cell size of 20 μm was used along both the axial and radial directions, which provides a spatial resolution of 30−50 cells in the reaction zone.

The inflow boundary of the computational domain was set some distance upstream of the burner exit and the co-flow tube exit plane (see H_j and H_c in Figure 1c). In this way, the fully developed laminar pipe flow profile could be applied at the jet inflow boundary. The inflow axial velocity was specified as

$$u(r) = 2U_{jet}(1 - r^2/R^2) \tag{10}$$

where $U_{jet} = \dot{m}/\pi R^2$ is the bulk flow velocity of the jet, with $\dot{m}$ being the mass flow rate of the fuel/air mixture. At the outer

https://dx.doi.org/10.1021/acs.energyfuels.0c03520
Energy Fuels 2021, 35, 7179−7192

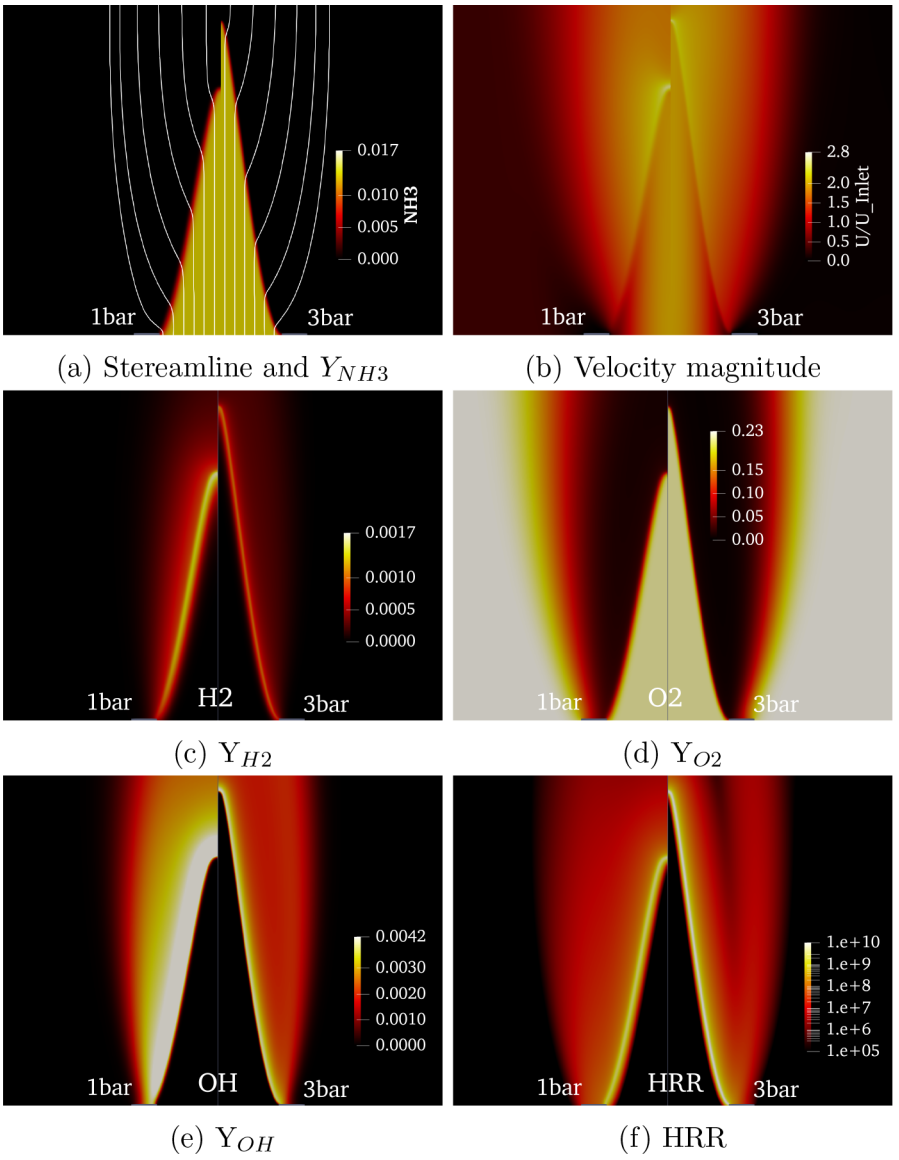

Figure 2. (a) Velocity streamlines and mass fraction of NH_3, (b) magnitude of velocity, (c) mass fraction of H_2, (d) mass fraction of O_2, (e) mass fraction of OH, and (f) HRR, from DNS of stoichiometric flames at p = 1 atm (case 8) and 3 atm (case 10), under an ammonia molar ratio of 0.2.

annular co-flow inlet, a small co-flow of air with a uniform axial velocity of $U_{\text{co-flow}}$ was applied.

Non-slip boundary conditions were employed at the burner wall. The burner wall was assumed to be adiabatic because the wall was not cooled. To explore the sensitivity of results to wall heat losses, simulations were also carried out under a constant wall temperature of 423 K, which is the same as the co-flow air temperature. At the downstream and the lateral far-field boundaries, the gradients of all dependent variables were set to zero.

Table 1 shows the experimental and computational cases, which cover a range of equivalence ratio (0.8−1.2), molar ratio of NH_3 to the total sum of NH_3 and CH_4 (0.2−0.8), and pressure (1−3 bar). In the experiments, the bulk flow velocity of the jet (U_{jet}) was adjusted so that the height of the flame remained approximately the same to allow for the PLIF measurements to be carried out in the same manner for all cases without having to adjust the laser sheet from one flame case to another. The co-flow air was used to burn out the fuel in the vessel. The fuel/air mixture through the jet and the co-flow was preheated to T_u = 423 K. To compare to the experiments and DNS results of the Bunsen-burner configuration, 1D detailed numerical simulations of the mixtures listed in Table 1 are performed on the freely propagating unstretched adiabatic premixed flame configuration using different chemical kinetic mechanisms.[35,36,40] The laminar flame speeds (S_L) obtained from the 1D simulations with the Okafor mechanism[40] are listed in Table 1.

Calculation of S_L from the DNS Results. From the DNS results, one can determine the laminar flame speed following the procedure described in ref 51. First, a local displacement speed (S_d) on an isosurface of the mass fraction of fuel (Y_f = $Y_{f,ref}$) can be defined as

$$S_{d,ref} = -\frac{1}{|\Delta Y_f|}\left(\frac{\partial Y_f}{\partial t} + \boldsymbol{u}\nabla Y_f\right)\Big|_{Y_f = Y_{f,ref}} \quad (11)$$

$S_{d,ref}$ is the local displacement speed of the isosurface of Y_f = $Y_{f,ref}$, which can be converted to the local displacement speed of the flame on the unburned side of the flame

https://dx.doi.org/10.1021/acs.energyfuels.0c03520
Energy Fuels 2021, 35, 7179−7192

$$S_d = \rho S_{d,ref}/\rho_u \quad (12)$$

where ρ is the local density on the isosurface of $Y_f = Y_{f,ref}$ and ρ_u is the density in the unburnt mixture. For a 1D planar flame, S_d is the laminar flame speed (S_L), which is a property of the mixture, independent of the flow. For multi-dimensional flames, this is however not true. Making use of eq 4, one can determine the laminar flame speed from the DNS data as follows:

$$S_L = S_d + \mathcal{L}\mathbb{K} \quad (13)$$

where the Markstein length $\mathcal{L}$ and the flame stretch rate $\mathbb{K}$ can be determined from the DNS data.

RESULTS AND DISCUSSION

All cases listed in Table 1 have been studied using PLIF imaging of NH and NO. Quantitative analysis of the NO mole fraction from PLIF data was performed for cases 1−6. Computational analysis includes DNS of the Bunsen flames and 1D numerical simulations in a planar freely propagating flame configuration for all cases listed in Table 1. In this paper, we focus on the analysis of the laminar flame speed and the NO distribution from experiments and numerical simulations. First, spatial distributions of species from PLIF measurements and numerical simulations are presented to analyze flame structures. The species are chosen to indicate the progress of ammonia oxidation, hydrogen production and oxidation, and formation of NO in different layers of the reaction zone. The laminar flame speed, determined from the experiments and numerical simulations, is then discussed, followed by a presentation of radial NO profiles.

Flame Structures. Figure 2 shows the flow field and the spatial mass fraction distributions of ammonia, hydrogen, oxygen, and OH radicals as well as the heat release rate (HRR) in the stoichiometric flame under ambient pressure of 1 bar (case 8) and 3 bar (case 10). The ammonia molar ratio in the ammonia/methane mixture is 0.2. Ammonia is seen to decrease rapidly across a thin layer, along with the consumption of oxygen and the formation of hydrogen across the layer. This reaction layer forms a premixed flame front. Hydrogen formed in the premixed flame front diffuses outward radially toward the ambient air and is consumed by reactions with oxidizers (such as OH radicals) on its way diffusing outward. Eventually, hydrogen is completely oxidized in the diffusion flame front as indicated by the HRR distribution. In the 3 bar flame, two distinctive HRR layers can be seen in the upper part of the flame (cf. Figure 2f), with the inner being the premixed flame layer and the outer being the diffusion flame layer. In the atmospheric flame, the two layers merge, as a result of a higher diffusion velocity than for the higher pressure flame.

In between the premixed flame front and the diffusion flame region, OH radicals are present and participate in reactions in the premixed flame and in the diffusion flame. The mass fraction of OH radicals in the premixed flame front is higher than in the diffusion flame. This gives rise to a much higher HRR in the premixed flame front than in the diffusion flame. CH_4 in the fuel/air mixture is oxidized at the premixed flame front, forming H_2 and CO, which are oxidized further in the diffusion flame and in the region between the premixed flame and the diffusion flame (for brevity, the results of CH_4 and CO are not shown here).

The flow streamlines in the unburned region upstream of the premixed flame front are parallel to the burner axis, and the velocity magnitude is essentially a function of the radial coordinate, independent of the axial coordinate (cf. panels a and b of Figure 2). Across the premixed flame front, the velocity increases rapidly and the streamlines are inclined toward the direction normal to the premixed flame front, owing to the gas expansion across the premixed flame. This result will be used later to determine the laminar flame speed from experimental data based on the formulation presented in eqs 5−9.

The pressure effect on the flame structures can be observed in Figure 2. The higher pressure flame (3 bar) has a lower jet velocity (Table 1) yet a longer flame. This indicates that the laminar flame speed of the higher pressure flame is lower than its lower pressure counterpart. The mass fraction of OH radicals in the higher pressure flame is also lower, which might be related to three-body radical recombination reactions, which are enhanced by higher pressures, e.g., $H + O_2 + M = HO_2 + M$. Competition of this reaction with the chain-branching reaction $H + O_2 = O + OH$ leads to a reduced concentration of radicals OH, H, and O. For this reason, the consumption rate of H_2 (by reaction with OH) in the premixed flame is presumably lower, and consequently, the HRR in the higher pressure flame would be lower. This affects the NO formation, as will be discussed below.

Figure 3 shows the spatial distribution of mass fractions of NH and NO from DNS and the corresponding PLIF signal for

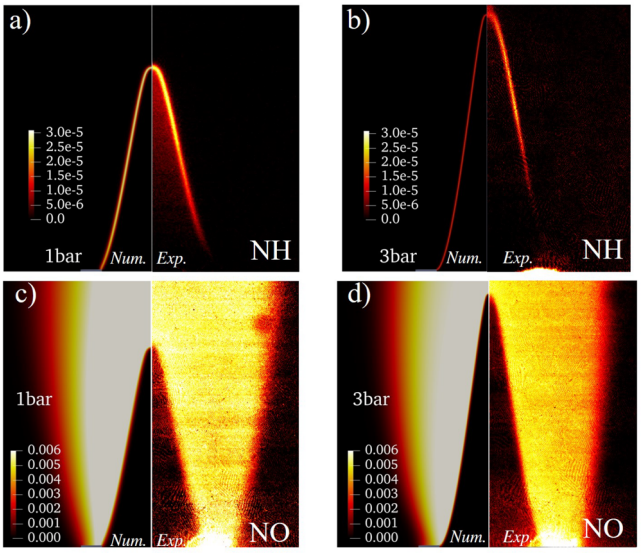

Figure 3. Spatial distribution of NH and NO of stoichiometric flame: (left) mass fractions from DNS and (right) PLIF signal intensity at (a and c) p = 1 atm (case 8) and (b and d) p = 3 atm (case 10). The color bar indicates mass fractions of NO from DNS.

the stoichiometric flames at pressures of 1 and 3 bar. NH is seen only in the premixed flame front, located in a thin layer. NO is present in the region between the premixed flame and the diffusion flame. The DNS results indicate that the atmospheric flame has significantly higher mass fractions of NH and NO than the 3 bar flame. This is largely due to the high mass fraction of radicals (H, O, and OH) in the atmospheric flame. A previous study of ammonia/hydrogen and ammonia/methane premixed flames indicated that NO

https://dx.doi.org/10.1021/acs.energyfuels.0c03520
Energy Fuels 2021, 35, 7179−7192

formation is highly sensitive to the reaction HNO + OH = NO + H_2O, being the largest contributor to NO production in several of their studied flames.[44] This reaction is suppressed at elevated pressure, also promoting the lower NO formation at 3 bar compared to 1 bar.

Laminar Flame Speed. The value of the laminar flame speed from the experiments is determined using the methodology described in eq 3 or 5. From the experiments, the bulk flow velocity U_{jet} and the flame height L_f (the axial distance from the tip of the flame to the burner exit plane) can be determined. Their values for the 10 experimental cases are shown in Table 1. The flame cone angle method (eq 3) has been frequently used in flame speed measurements; however, the results are subject to uncertainties caused by the presence of the flame stretch[51,56−58] and non-uniform flow velocity in front of the flame. The effect of the flame stretch and non-uniform flow of the unburned mixture are taken into account in eqs 5. Figure 4 shows a comparison between the flame front

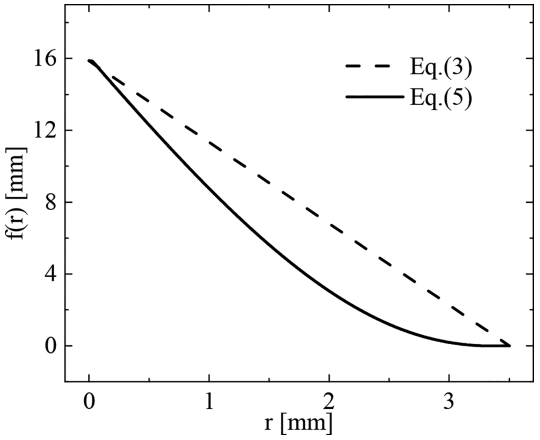

Figure 4. Flame front profiles for case 1 determined using different methods.

function $x = f(r)$ described using eqs 2 and 5. As seen, eq 5 yields a more accurate prediction of the flame front than eq 2 when comparing to the experimental results (as indicated by the NH distributions).

Figure 5 shows the values of the laminar flame speed evaluated from the experiments using eq 3 or 5. The values from eq 5 are consistently higher than those from eq 3. The 1D numerical results from the mechanism of Okafor et al.,[40] Li et al.,[36] and Glarborg et al.[35] agree well with the experimental results from eq 5; however, they slightly overpredict values for flames of higher fractions of ammonia (cases 5 and 6), especially the latter mechanism. It is worth noticing that the numerical results from different mechanisms agree very well with each other for the atmospheric flames (cases 1, 7, and 8) while differing more at elevated pressure.

The DNS results were also used to determine the laminar flame speed, using the flame cone-angle method (eq 3). The DNS results are in good agreement with the experiments (cf. Figure 5), slightly underpredicting values for flames of low ammonia content (cases 1, 2, 3, 7, 9, and 10). A good agreement between the experimental results and DNS results indicates that the prediction of the flame height is good. As indicated in Figure 2, the flame shape from DNS also agrees well with the experiments (cf., the NH distribution). This confirms the accuracy of the inflow boundary condition.

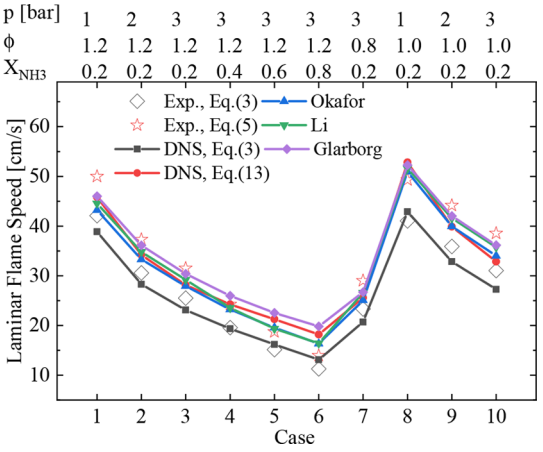

Figure 5. Laminar flame speed from experiments and DNS of Bunsen flames, and from 1D numerical simulations of planar unstretched flames.

When using eq 5 to determine the laminar flame speed (by solving eqs 5−9), an important input parameter is the Markstein length ($\mathcal{L}$). The value of the Markstein length can be determined from theoretical analysis,[59,60] but it is found here that the theoretically estimated value of $\mathcal{L}$ is about 10-fold the value determined from the DNS results.

Equations 11−13 can be used to determine the values of the laminar flame speed and Markstein length. Figure 6 shows the

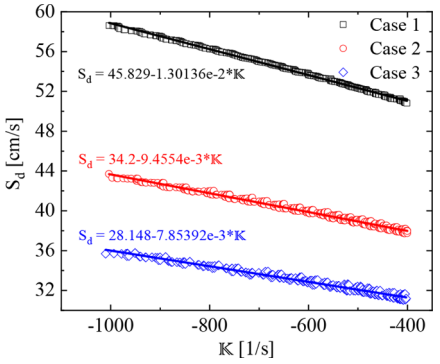

Figure 6. Local flame displacement speed S_d along the flame height of cases 1−3, expressed as a function of the local stretch rate $\mathbb{K}$.

value of S_d along the flame height (around mid-flame height). It is clear that, in the investigated region of the flame, S_d is a linear function of the flame stretch rate $\mathbb{K}$, with the slope being the Markstein length. The value of $\mathcal{L}$ for the 10 experimental cases determined using eqs 11−13 are given in Table 1. They are used in calculating the unstretched laminar flame speed using eq 5 shown in Figure 5. From eq 13, the unstretched laminar flame speed can be determined from the DNS results. As shown in Figure 5, DNS-predicted S_L from eq 13 agrees well with the corresponding experimental results as well as with the 1D numerical results from the same mechanism (i.e., the Okafor mechanism[40]). However, the DNS results with the flame cone angle method consistently underpredicted the laminar flame speed. This is attributed to the effect of the flame stretch.

For comparison, Table 1 also shows the value of Markstein length $\mathcal{L}$ determined from the experimental flame front, e.g., the NH PLIF field. First, a flame front function $x = f(r)$ is

https://dx.doi.org/10.1021/acs.energyfuels.0c03520
Energy Fuels 2021, 35, 7179−7192

determined from the NH PLIF field. Using eqs 6−8, the flame stretch rate $\mathbb{K}$ can be computed. From eq 5, with a given S_L (i.e., the value of S_L given in Table 1), $\mathcal{L}$ is determined. In general, the Markstein length from the experiments is on the same order of magnitude as that from DNS, and the two lengths follow a similar trend when varying the flame conditions.

Uncertainties of the S_L Measurement Using the Bunsen Burner. Errors in the measured laminar flame speed may be classified to two types: random errors and systematic errors. Random errors may stem from the readings of the mass flow rate, error in the ambient temperature and reactant flow temperature, and ambient pressure fluctuations. The effects of the random errors and fluctuations on the laminar flame speed are evaluated in the post-processing and expressed in terms of the standard deviation of the laminar flame speed. The results are shown in Table 2. It is seen that the largest standard deviation of the laminar flame speed is 0.6 cm/s (in case 8), which is about 1.2% of the measured laminar flame speed.

Table 2. Laminar Flame Speed (S_L in cm/s) from DNS using the Okafor Mechanism,[40] 1D Numerical Simulation Using the Okafor Mechanism, and Experiments[a]

	DNS		1D		experiment		
case	eq 3	eq 13	Okafor	ε_{S_L}	eq 3	eq 5	σ_{S_L}
1	38.87	45.83	43.20	2.63	42.08	50.69	0.29
2	28.29	34.20	33.28	0.92	30.56	39.19	0.31
3	23.10	28.15	27.91	0.24	25.51	33.06	0.27
4	19.34	24.23	23.22	1.01	19.56	25.25	0.07
5	16.18	21.25	19.57	1.68	15.14	18.89	0.08
6	13.10	18.20	16.33	1.87	11.28	13.76	0.29
7	20.70	25.57	25.07	0.50	23.34	28.95	0.22
8	42.89	52.80	50.91	1.89	41.04	48.97	0.60
9	32.85	39.86	39.95	0.09	35.90	45.96	0.14
10	27.27	32.85	34.00	1.15	31.05	39.12	0.39

[a] ε_{S_L} (cm/s) is the difference between the laminar flame speed from the DNS of the Bunsen flame (eq 13) and that from the 1D numerical simulation, which indicates the systematic error of the Bunsen burner method for determination of the laminar flame speed. The standard deviation (σ_{S_L}, cm/s) is for the experimental results with eq 5, which indicates the error in the measurements as a result of random variation of operating conditions.

Systematic errors of the laminar flame speed may stem from the wall heat loss (because adiabatic flame speed is sought in the measurements), the buoyancy effect associated with the Bunsen flame (which is absent in the idealized 1D freely propagating flame), and the difference of burner configuration. The buoyancy effect and wall heat loss effect are investigated using DNS. It is found that the flame structure (e.g., NH distribution) is identical with and without the inclusion of the buoyancy force in the DNS. To investigate the effect of wall heat losses, DNS with two different wall boundary conditions has been carried out for the lowest flame speed case (case 6): a constant wall temperature (423 K, the same as the reactant temperature) and an adiabatic wall. The flame height from the two boundary conditions varied about 0.2 mm, which results in a difference in the laminar flame speed of about 0.2 cm/s, based on the method described by eq 3, which is about 1% of the value of the laminar flame speed.

The systematic error may arise due to the difference of the Bunsen burner configuration from that of the idealized 1D freely propagating planar flame. This error is evaluated by comparing the results from the 1D numerical simulation and that of Bunsen burner DNS, both with the same chemical kinetic mechanism (the Okafor mechanism). The results are shown in Table 2. It is seen that the error is small for most of the flame cases. The largest relative error is 10%, which occurs in the flame case with the lowest flame speed. The largest absolute error is 2.63 cm/s, occurring in case 1, which is about 6% of the value of the laminar flame speed.

NO Emission. Figures 7 and 8 show the radial profiles of the NO mole fraction for flames of equivalence ratio ϕ = 1.2 (cases 1−6), at height 10 mm above the burner, obtained from numerical simulations and PLIF experiments. The rapid increase of NO around r = 1−1.5 mm is due to the NO formation at the premixed flame front. Because the oxidation of NH_3 occurs in a very thin layer (cf. Figure 2), the formation of NO is also very rapid. Qualitatively, DNS captures the trends of the experimental profiles well. The NO profile shows a steeper gradient toward the premixed flame reaction zone for cases 1−3 with 20% NH_3 in the fuel as well as for case 4. For cases 5 and 6, with 60 and 80% NH_3 in the fuel, respectively, the gradient is lower, which is, however, overpredicted in the numerical simulations. A local minimum of the NO mole fraction at radial positions from 2 to 3 mm can be observed for cases 4−6 in both PLIF data and DNS results, which corresponds to the low HRR and low OH radical concentration region between the premixed and diffusion flames, as discussed previously (panels e and f of Figure 2). Quantitatively, experimental data and DNS profiles are generally on par with each other, with differences of up to 20% in the NO mole fraction. The uncertainty of the experimental data is indicated by the error bar in Figure 7 (case 2). Considering the uncertainty range, it is clear that the experimental data and DNS predictions follow a consistent trend.

Duynslaegher et al. reported a rather weak pressure dependence of NO formation in NH_3 combustion.[69] For 20% NH_3 in the fuel (cf. Figure 7), NO mole fractions from DNS and PLIF data show a moderate decrease with increasing pressure from 1 to 3 bar (although the PLIF data show a higher mole fraction at 2 bar than at 1 bar). The moderate decrease of the NO mole fraction with increasing pressure suggests that NO formation becomes inhibited as the pressure increases. From the OH radical field discussed in Figure 2e, this appears to be due to the increased effect of three-body radical recombination reactions that result in decreasing radical concentrations (H, O, and OH) with increasing pressure.

For cases 3−6 (Figures 7 and 8), the NH_3 molar ratio increases from 20 to 80%, while the pressure is constant at 3 bar. Comparing this sequence of results shows a consistent decrease in the NO mole fraction in both experiments and DNS. This indicates that, under the present conditions, a higher ammonia ratio in the ammonia/methane/air mixture can lead to reduced NO emission. Ramos et al.[43] also found similar trends of reduction in NO_x for stoichiometric ammonia/methane/air flames at atmospheric pressure, reporting decreasing NO_x emissions with an increasing ammonia ratio in the fuel/air mixture. Analysis of the present DNS results from the Okafor mechanism[40] show that, with a higher ammonia ratio in the fuel, the NO reduction reaction H + NO = HNO is enhanced, which partly contributes to the

https://dx.doi.org/10.1021/acs.energyfuels.0c03520
Energy Fuels 2021, 35, 7179−7192

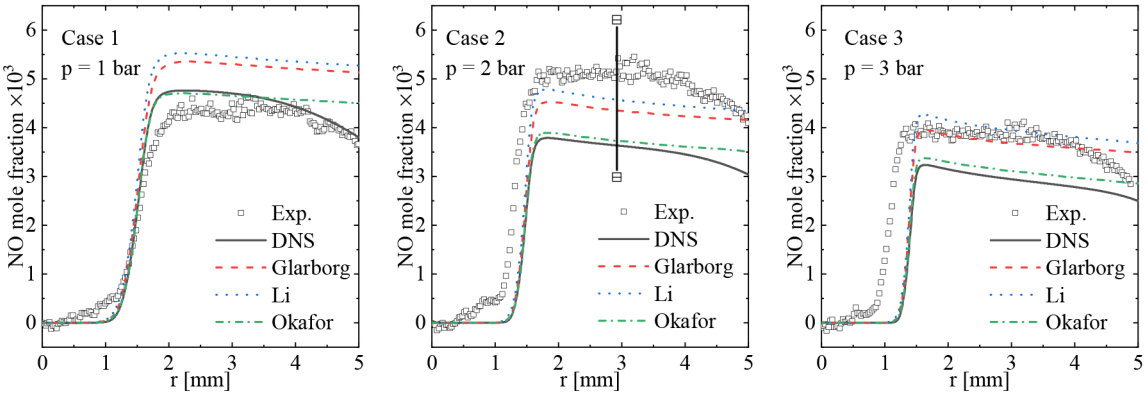

Figure 7. Mole fractions of NO obtained from DNS (solid lines), PLIF experiments (square symbols), and numerical simulations of 1D freely propagating premixed flames with ammonia molar ratio (X_{NH_3}) of 0.2, equivalence ratio of 1.2, and pressure of 1−3 bar. The 1D flame simulations were made using mechanisms of Glarborg et al.[35] (dashed line), Li et al.[36] (dotted line), and Okafor et al.[40] (dash-dotted line). The vertical axis shows the value of mole fractions multiplied by 1000.

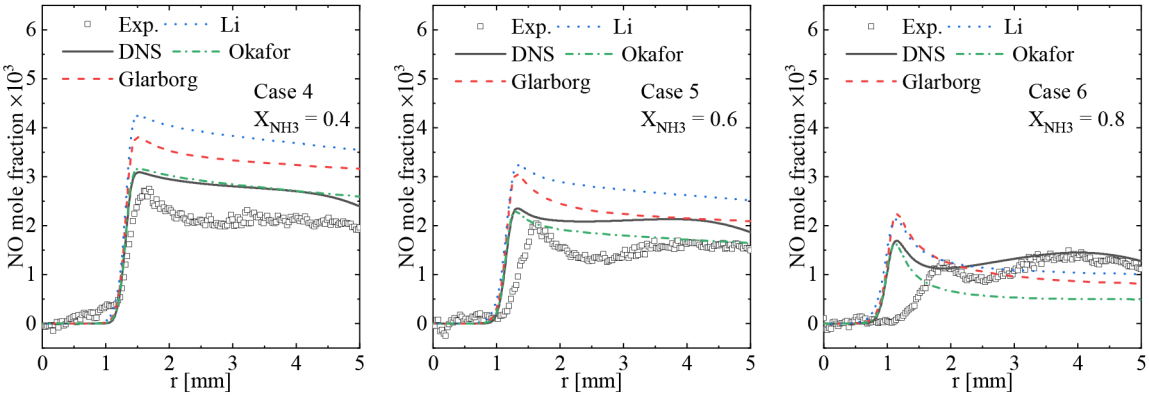

Figure 8. Mole fractions of NO obtained from DNS (solid lines), PLIF experiments (square symbols), and numerical simulations of 1D freely propagating premixed flames under conditions of pressure of 3 bar, equivalence ratio of 1.2, and ammonia molar ratio of 0.4−0.8. The 1D flame simulations were made using mechanisms of Glarborg et al.[35] (dashed line), Li et al.[36] (dotted line), and Okafor et al.[40] (dash-dotted line). The vertical axis shows the value of mole fractions multiplied by 1000.

decreasing NO emission with an increasing ammonia molar ratio in the fuel.

NO formation rates from DNS indicate that, in all cases studied, NO formation mainly occurs in the premixed flame front. The diffusion flame does not significantly contribute to the NO formation. However, this cannot explain the two NO peaks observed in cases 5 and 6 (cf. Figure 8). To gain insight into this phenomenon, Figure 9 shows the spatial distribution of the NO mole fraction in two fuel-rich flames (cases 3 and 6) with an equivalence ratio of ϕ = 1.2 and pressure of 3 bar. With a higher ammonia ratio (case 6), the NO distribution shows rather different characteristics: at the premixed flame front (upper part of the flame), a higher NO mass fraction is observed in a thin layer, and near the burner rim, the highest NO concentration is observed in a broad region in between the diffusion flame front and the premixed flame front. Reaction rate analysis indicates that, for case 6, the two most important reactions that contribute to the formation of NO are $N_2O + H = NO + NH$ and $HNO + H = NO + H_2$. While HNO is found only in the premixed flame layer, N_2O can be found in both the premixed flame layer and the diffusion flame layer. Near the burner rim, these two layers are closer to each other; thus, the local formation rate of NO is higher than that in the downstream region as a result of the summation of the rates

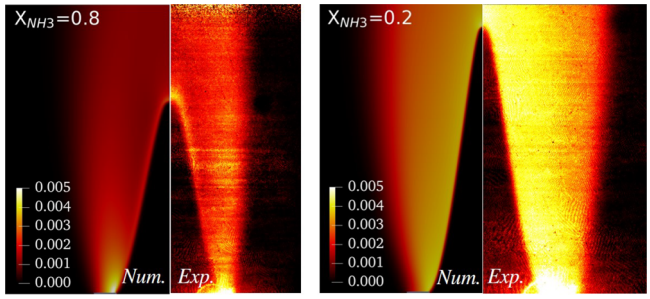

Figure 9. Spatial distribution of NO of the fuel-rich flames with ϕ = 1.2, pressure of 3 bar, and ammonia molar ratio of 0.8 (case 6) and 0.2 (case 3). In each panel, the left is from DNS and the right is from PLIF experiments. The color bar indicates NO mass fractions from DNS.

from these two reactions in the near burner region. Furthermore, for case 6, reaction $N_2 + O = NO + N$ is also important near the burner rim, where the concentration of O radicals is higher in the diffusion flame layer under fuel-rich conditions. This contributes further to the high NO concentration near the burner rim of case 6.

As a result of the reduced diffusion coefficient at high pressures, the diffusion of NO formed in the premixed flame is

https://dx.doi.org/10.1021/acs.energyfuels.0c03520
Energy Fuels 2021, 35, 7179−7192

slower toward the diffusion flame layer. The NO field in case 6 (Figure 9) shows that the peak of NO in the outer diffusion flame layer is due to the convective transport of NO generated in the upstream region near the burner rim. This characteristic can be observed in both the DNS and PLIF results. As discussed earlier, at a low ammonia ratio case (case 3), the formation rate of NO is higher (than that with a higher ammonia ratio) in the premixed flame front, which results in a higher NO mole fraction at the premixed flame front (cf. Figure 8). Thus, diffusion from the premixed flame to the diffusion flame is enhanced, resulting in a more uniform distribution of NO in the region between the premixed flame front and the diffusion flame front.

One major difference between the 1D result and the DNS result can be found at large radial positions. As a result of the presence of the diffusion flame layer in the DNS and experiments, which is absent in the 1D configuration, the local minimum of NO mole fraction in cases 5 and 6 does not exist in the 1D results. Another noticeable difference in the 1D and DNS/experimental results lies in the decrease of NO at radial positions $r > 4$ mm. This is due to the ambient air dilution in the jet flame configuration, which is not modeled in the 1D simulations.

Figures 7 and 8 also present NO profiles predicted from simulations of 1D, freely propagating premixed flames, using different chemical kinetic mechanisms. The results from DNS and 1D numerical simulations using the Okafor mechanism[40] agree very well in the premixed flame region, indicating that the flame stretch at the height of 10 mm has rather minor impact on the NO formation process in the premixed flame region. The NO mole fractions predicted by the Glarborg et al. and Li et al. mechanisms are higher than that from the Okafor mechanism. The difference in the NO profiles from 1D numerical simulations using different chemical mechanisms is nevertheless rather large, indicating that current chemical kinetic mechanisms for ammonia combustion require more development for accurate prediction of NO formation.

CONCLUDING REMARKS

The structure and laminar flame speed have been investigated for laminar premixed ammonia/methane/air jet flames in a pressurized constant-pressure vessel under a range of equivalence ratios (0.8−1.2), pressures (1−3 bar), and ammonia/methane molar ratios (0.2−0.8). Measurements were made using PLIF of NO and NH. DNS of the jet flames was performed, along with 1D modeling of unstretched planar flames using three recently developed chemical kinetic mechanisms. DNS and PLIF results show that flames in an ambient co-flow of air under stoichiometric or fuel-rich conditions exhibit a dual flame structure, with an inner premixed flame and an outer diffusion flame. Under the currently studied equivalence ratios ($\phi \leq 1.2$), NH_3 and CH_4 are oxidized in the inner premixed flame, while combustion intermediates (e.g., H_2) formed in the premixed flame diffuse toward the ambient air flow, establishing a diffusion flame where the intermediates are finally oxidized. The main findings are summarized as follows: (1) The inner premixed flame and outer diffusion flame show significant interaction as a result of the diffusion of species and heat between the two flames. The interaction is weakened as the pressure increases as a result of a reduced diffusion velocity. It is found that NO is mainly formed in the inner premixed flames, while the diffusion flame also contributes to the formation of NO. In the inner premixed flame, a thin layer of NH is identified and OH radicals reach their peak level. Reactions of fuel NO formation, through the HNO route in the premixed flame, are deemed to be responsible of the NO peak in this layer. Under elevated pressures, a dual-peak NO profile has been observed in the PLIF data and DNS results, which is due to the convective transport of NO from the upstream region near the burner. NO formation in the diffusion flame front is negligible in comparison to that in the premixed flame front. (2) NO emissions are shown to be suppressed at elevated pressures. This can be attributed to the enhanced three-body radical recombination reactions that suppress the radical formation in the inner premixed flames, which subsequently suppress the NO formation rate. NO emission is also suppressed with an increasing ammonia to methane ratio in the fuel/air mixture under the currently investigated range of the ammonia molar range ($X_{NH_3} \leq 0.8$). The main reason behind this is the enhanced NO reduction reaction (H + NO = HNO) at high ammonia ratios. (3) A novel method is presented and used to determine the laminar flame speed using Bunsen burners. The method takes into account non-uniform flow velocity in the unburned mixture in front of the premixed flame as well as the local flame stretch rate pertaining to the Bunsen burner flames. The method is analyzed using the DNS results and compared to the conventional flame cone-angle method. A significantly improved accuracy of the laminar flame speed measured using Bunsen burners with the new method is found in comparison to the flame cone-angle method. (4) The laminar flame speed under varying equivalence ratio, pressure, and ammonia/methane ratio is determined using the new method. NH profiles were used as flame front markers, and the data are compared to predictions from three recent chemical kinetic mechanisms, with overall good agreement being observed. Predictions of the mechanisms show close agreement between one another under most conditions studied, with the largest discrepancy found at high ammonia ratio conditions. (5) Although the recent chemical kinetic mechanisms show consistent predictions of the laminar flame speed, their predictions of NO formation in the current flames scatter significantly. This calls for further development of the current chemical kinetic mechanisms for improved calculation of NO profiles. Although a significant influence of the outer diffusion flame on NO formation is observed in the present Bunsen burner rig, the outer diffusion flame does not show a strong impact on the laminar flame speed of the inner premixed flame. This allows for the studies of moderately fuel-rich laminar flames (under the present equivalence ratio range) using Bunsen burners. It is expected that, under high equivalence ratio conditions (close to the fuel-rich flammability limit), the outer diffusion flame should exert a more significant impact on the inner premixed flames.

AUTHOR INFORMATION

Corresponding Authors

Xue-Song Bai − *Division of Fluid Mechanics, Lund University, 221 00 Lund, Sweden*; Phone: +46-0-46-2224860; Email: xue-song.bai@energy.lth.se; Fax: +46-0-46-2224717

Christian Brackmann − *Division of Combustion Physics, Lund University, 221 00 Lund, Sweden*; Email: christian.brackmann@forbrf.lth.se

https://dx.doi.org/10.1021/acs.energyfuels.0c03520
Energy Fuels 2021, 35, 7179−7192

Authors

Rodolfo C. Rocha − *Division of Fluid Mechanics, Lund University, 221 00 Lund, Sweden; Instituto de Engenharia Mecânica (IDMEC), Instituto Superior Técnico (IST), Universidade de Lisboa, 1049-001 Lisboa, Portugal*

Shenghui Zhong − *Division of Fluid Mechanics, Lund University, 221 00 Lund, Sweden; State Key Laboratory of Engines, Tianjin University, Tianjin 300350, People's Republic of China*

Leilei Xu − *Division of Fluid Mechanics, Lund University, 221 00 Lund, Sweden;* orcid.org/0000-0001-6074-2039

Mário Costa − *Instituto de Engenharia Mecânica (IDMEC), Instituto Superior Técnico (IST), Universidade de Lisboa, 1049-001 Lisboa, Portugal;* orcid.org/0000-0002-3118-2762

Xiao Cai − *Division of Combustion Physics, Lund University, 221 00 Lund, Sweden*

Haisol Kim − *Division of Combustion Physics, Lund University, 221 00 Lund, Sweden*

Zhongshan Li − *Division of Combustion Physics, Lund University, 221 00 Lund, Sweden;* orcid.org/0000-0002-0447-2748

Marcus Aldén − *Division of Combustion Physics, Lund University, 221 00 Lund, Sweden*

Complete contact information is available at: https://pubs.acs.org/10.1021/acs.energyfuels.0c03520

Notes

The authors declare no competing financial interest.

The code implementation of species detailed transport properties in OpenFOAM (version7) is available at https://github.com/ZSHtju/reactingDNS_OpenFOAM.

■ ACKNOWLEDGMENTS

This work is dedicated to Prof. Mário Costa, our dear supervisor, friend, and colleague, who passed away in June 2020. Mário initiated a close collaboration between Lund University and IST in many projects. In the last few years, Mário devoted his strong passion to measurements and simulations of ammonia combustion, in search for developing a renewable carbon-free fuel for a future energy system. This work was partly sponsored by the Swedish Research Council (VR), Knut and Alice Wallenberg Foundation within the Project COCALD, the European Research Council (Advanced Grant TUCLA, 669466), the Swedish Foundation of Strategic Research (Project ITM17-0313), and the Swedish Energy Agency (STEM) through the National Center for Combustion Science and Technology (CECOST, Project KC-CECOST 22538-4). Rodolfo C. Rocha acknowledges Fundação para a Ciência e a Tecnologia for the provision of Scholarship SFRH/BD/143971/2019 and through IDMEC, under LAETA, for the provision of Project UIDB/EMS/50022/2020. Shenghui Zhong was sponsored by the China Scholarship Council (CSC). The simulations are performed on resources provided by the Swedish National Infrastructure for Computing (SNIC) at HPC2N and NSC.

■ REFERENCES

(1) International Energy Agency (IEA). *World Energy Outlook 2019*; IEA: Paris, France, 2019; https://www.iea.org/reports/world-energy-outlook-2019 (accessed Oct 11, 2020).

(2) Valera-Medina, A.; Xiao, H.; Owen-Jones, M.; David, W.; Bowen, P. Ammonia for power. *Prog. Energy Combust. Sci.* **2018**, *69*, 63−102.

(3) Kobayashi, H.; Hayakawa, A.; Somarathne, K. K. A.; Okafor, E. C. Science and technology of ammonia combustion. *Proc. Combust. Inst.* **2019**, *37*, 109−133.

(4) Advanced Research Projects Agency−Energy (ARPA-E). *Renewable Energy to Fuels through Utilization of Energy-Dense Liquids Transportation Fuels*; ARPA-E: Washington, D.C., 2016; https://arpa-e.energy.gov/technologies/programs/refuel (accessed Oct 11, 2020).

(5) Bañares-Alcántara, R.; Dericks, G., III; Fiaschetti, M.; Grünewald, P.; Lopez, J. M.; Tsang, E.; Yang, A.; Ye, L.; Zhao, S. *Analysis of Islanded Ammonia-Based Energy Storage Systems*; University of Oxford: Oxford, U.K., 2015.

(6) Mørch, C.; Bjerre, A.; Gøttrup, M.; Sorenson, S.; Schramm, J. Ammonia/hydrogen mixtures in an SI-engine: Engine performance and analysis of a proposed fuel system. *Fuel* **2011**, *90*, 854−864.

(7) Duynslaegher, C. Experimental and numerical study of ammonia combustion. Ph.D. Thesis, Université catholique de Louvain, Louvain, Belgium, 2011.

(8) Westlye, F. R.; Ivarsson, A.; Schramm, J. Experimental investigation of nitrogen based emissions from an ammonia fueled SI-engine. *Fuel* **2013**, *111*, 239−247.

(9) Ryu, K.; Zacharakis-Jutz, G. E.; Kong, S.-C. Performance enhancement of ammonia-fueled engine by using dissociation catalyst for hydrogen generation. *Int. J. Hydrogen Energy* **2014**, *39*, 2390−2398.

(10) Lhuillier, C.; Brequigny, P.; Contino, F.; Mounaïm-Rousselle, C. Experimental investigation on ammonia combustion behavior in a spark-ignition engine by means of laminar and turbulent expanding flames. *Proc. Combust. Inst.* **2020**, DOI: 10.1016/j.proci.2020.08.058.

(11) Reiter, A. J.; Kong, S.-C. Demonstration of Compression-Ignition Engine Combustion Using Ammonia in Reducing Greenhouse Gas Emissions. *Energy Fuels* **2008**, *22*, 2963−2971.

(12) Ryu, K.; Zacharakis-Jutz, G. E.; Kong, S.-C. Performance characteristics of compression-ignition engine using high concentration of ammonia mixed with dimethyl ether. *Appl. Energy* **2014**, *113*, 488−499.

(13) Lee, D.; Song, H. H. Development of combustion strategy for the internal combustion engine fueled by ammonia and its operating characteristics. *J. Mech. Sci. Technol.* **2018**, *32*, 1905−1925.

(14) MAN Energy Solutions. *Engineering the Future Two-Stroke Green-Ammonia Engine*; MAN Energy Solutions: Copenhagen, Denmark, 2019.

(15) Comotti, M.; Frigo, S. Hydrogen generation system for ammonia-hydrogen fuelled internal combustion engines. *Int. J. Hydrogen Energy* **2015**, *40*, 10673−10686.

(16) Kurata, O.; Iki, N.; Matsunuma, T.; Inoue, T.; Tsujimura, T.; Furutani, H.; Kobayashi, H.; Hayakawa, A. Performances and emission characteristics of NH_3−air and NH_3−CH_4−air combustion gas-turbine power generations. *Proc. Combust. Inst.* **2017**, *36*, 3351−3359.

(17) Hayakawa, A.; Arakawa, Y.; Mimoto, R.; Somarathne, K. K. A.; Kudo, T.; Kobayashi, H. Experimental investigation of stabilization and emission characteristics of ammonia/air premixed flames in a swirl combustor. *Int. J. Hydrogen Energy* **2017**, *42*, 14010−14018.

(18) Okafor, E. C.; Somarathne, K. K. A.; Hayakawa, A.; Kudo, T.; Kurata, O.; Iki, N.; Kobayashi, H. Towards the development of an efficient low-NO_x ammonia combustor for a micro gas turbine. *Proc. Combust. Inst.* **2019**, *37*, 4597−4606.

(19) Kurata, O.; Iki, N.; Inoue, T.; Matsunuma, T.; Tsujimura, T.; Furutani, H.; Kawano, M.; Arai, K.; Okafor, E. C.; Hayakawa, A.; Kobayashi, H. Development of a wide range-operable, rich-lean low-NO_x combustor for NH_3 fuel gas-turbine power generation. *Proc. Combust. Inst.* **2019**, *37*, 4587−4595.

(20) Valera-Medina, A.; Morris, S.; Runyon, J.; Pugh, D.; Marsh, R.; Beasley, P.; Hughes, T. Ammonia, Methane and Hydrogen for Gas Turbines. *Energy Procedia* **2015**, *75*, 118−123.

(21) Valera-Medina, A.; Gutesa, M.; Xiao, H.; Pugh, D.; Giles, A.; Goktepe, B.; Marsh, R.; Bowen, P. Premixed ammonia/hydrogen swirl combustion under rich fuel conditions for gas turbines operation. *Int. J. Hydrogen Energy* **2019**, *44*, 8615−8626.
(22) Valera-Medina, A.; Pugh, D.; Marsh, P.; Bulat, G.; Bowen, P. Preliminary study on lean premixed combustion of ammonia-hydrogen for swirling gas turbine combustors. *Int. J. Hydrogen Energy* **2017**, *42*, 24495−24503.
(23) Pugh, D.; Bowen, P.; Valera-Medina, A.; Giles, A.; Runyon, J.; Marsh, R. Influence of steam addition and elevated ambient conditions on NO_x reduction in a staged premixed swirling NH_3/H_2 flame. *Proc. Combust. Inst.* **2019**, *37*, 5401−5409.
(24) Franco, M. C.; Rocha, R. C.; Costa, M.; Yehia, M. Characteristics of NH_3/H_2/air flames in a combustor fired by a swirl and bluff-body stabilized burner. *Proc. Combust. Inst.* **2020**, DOI: 10.1016/j.proci.2020.06.141.
(25) Rocha, R. C.; Costa, M.; Bai, X.-S. Combustion and Emission Characteristics of Ammonia under Conditions Relevant to Modern Gas Turbines. *Combust. Sci. Technol.* **2020**, *0*, 1−20.
(26) Miller, J. A.; Bowman, C. T. Mechanism and modeling of nitrogen chemistry in combustion. *Prog. Energy Combust. Sci.* **1989**, *15*, 287−338.
(27) Skreiberg, Ø.; Kilpinen, P.; Glarborg, P. Ammonia chemistry below 1400 K under fuel-rich conditions in a flow reactor. *Combust. Flame* **2004**, *136*, 501−518.
(28) Dagaut, P.; Glarborg, P.; Alzueta, M. U. The oxidation of hydrogen cyanide and related chemistry. *Prog. Energy Combust. Sci.* **2008**, *34*, 1−46.
(29) Konnov, A. Implementation of the NCN pathway of prompt-NO formation in the detailed reaction mechanism. *Combust. Flame* **2009**, *156*, 2093−2105.
(30) Tian, Z.; Li, Y.; Zhang, L.; Glarborg, P.; Qi, F. An experimental and kinetic modeling study of premixed NH_3/CH_4/O_2/Ar flames at low pressure. *Combust. Flame* **2009**, *156*, 1413−1426.
(31) Mendiara, T.; Glarborg, P. Ammonia chemistry in oxy-fuel combustion of methane. *Combust. Flame* **2009**, *156*, 1937−1949.
(32) Klippenstein, S. J.; Harding, L. B.; Glarborg, P.; Miller, J. A. The role of NNH in NO formation and control. *Combust. Flame* **2011**, *158*, 774−789.
(33) Duynslaegher, C.; Contino, F.; Vandooren, J.; Jeanmart, H. Modeling of ammonia combustion at low pressure. *Combust. Flame* **2012**, *159*, 2799−2805.
(34) Song, Y.; Hashemi, H.; Christensen, J. M.; Zou, C.; Marshall, P.; Glarborg, P. Ammonia oxidation at high pressure and intermediate temperatures. *Fuel* **2016**, *181*, 358−365.
(35) Glarborg, P.; Miller, J. A.; Ruscic, B.; Klippenstein, S. J. Modeling nitrogen chemistry in combustion. *Prog. Energy Combust. Sci.* **2018**, *67*, 31−68.
(36) Li, R.; Konnov, A. A.; He, G.; Qin, F.; Zhang, D. Chemical mechanism development and reduction for combustion of NH_3/H_2/CH_4 mixtures. *Fuel* **2019**, *257*, 116059.
(37) da Rocha, R. C.; Costa, M.; Bai, X.-S. Chemical kinetic modelling of ammonia/hydrogen/air ignition, premixed flame propagation and NO emission. *Fuel* **2019**, *246*, 24−33.
(38) Mathieu, O.; Petersen, E. L. Experimental and modeling study on the high-temperature oxidation of Ammonia and related NO_x chemistry. *Combust. Flame* **2015**, *162*, 554−570.
(39) Otomo, J.; Koshi, M.; Mitsumori, T.; Iwasaki, H.; Yamada, K. Chemical kinetic modeling of ammonia oxidation with improved reaction mechanism for ammonia/air and ammonia/hydrogen/air combustion. *Int. J. Hydrogen Energy* **2018**, *43*, 3004−3014.
(40) Okafor, E. C.; Naito, Y.; Colson, S.; Ichikawa, A.; Kudo, T.; Hayakawa, A.; Kobayashi, H. Experimental and numerical study of the laminar burning velocity of CH_4-NH_3-air premixed flames. *Combust. Flame* **2018**, *187*, 185−198.
(41) Smith, G. P.; Golden, D. M.; Frenklach, M.; Moriarty, N. W.; Eiteneer, B.; Goldenberg, M.; Bowman, C. T.; Hanson, R. K.; Song, S.; Gardiner, W. C., Jr.; Lissianski, V. V.; Qin, Z. *GRI-Mech 3.0*; Gas Research Institute (GRI): Chicago, IL, 1999; http://combustion.berkeley.edu/gri-mech/.
(42) Brackmann, C.; Alekseev, V. A.; Zhou, B.; Nordstrom, E.; Bengtsson, P. E.; Li, Z. S.; Aldén, M.; Konnov, A. A. Structure of premixed ammonia plus air flames at atmospheric pressure: Laser diagnostics and kinetic modeling. *Combust. Flame* **2016**, *163*, 370−381.
(43) Filipe Ramos, C.; Rocha, R. C.; Oliveira, P. M. R.; Costa, M.; Bai, X.-S. Experimental and kinetic modelling investigation on NO, CO and NH_3 emissions from NH_3/CH_4/air premixed flames. *Fuel* **2019**, *254*, 115693.
(44) Rocha, R. C.; Ramos, C. F.; Costa, M.; Bai, X.-S. Combustion of NH_3/CH_4/Air and NH_3/H_2/Air Mixtures in a Porous Burner: Experiments and Kinetic Modeling. *Energy Fuels* **2019**, *33*, 12767−12780.
(45) Chou, M. S.; Dean, A. M.; Stern, D. Laser-Induced Fluorescence and Absorption-Measurements of NO in NH_3-O_2 and CH_4-Air Flames. *J. Chem. Phys.* **1983**, *78*, 5962−5970.
(46) Li, B.; He, Y.; Li, Z. S.; Konnov, A. A. Measurements of NO concentration in NH_3-doped CH_4 + air flames using saturated laser-induced fluorescence and probe sampling. *Combust. Flame* **2013**, *160*, 40−46.
(47) Brackmann, C.; Nilsson, E. J. K.; Naucler, J. D.; Aldén, M.; Konnov, A. A. Formation of NO and NH in NH_3-doped CH_4 + N_2 + O_2 flame: Experiments and modelling. *Combust. Flame* **2018**, *194*, 278−284.
(48) Venizelos, D. T.; Sausa, R. C. Detailed chemical kinetics studies of an NH_3/N_2O/Ar flame by laser-induced fluorescence, mass spectrometry, and modeling. *Proc. Combust. Inst.* **2000**, *28*, 2411−2418.
(49) Venizelos, D. T.; Sausa, R. C. Laser-induced fluorescence, mass spectrometric, and modeling studies of neat and NH_3-Doped H_2/N_2O/Ar flames. *Combust. Flame* **1998**, *115*, 313−326.
(50) Joo, P. H.; Gao, J.; Li, Z.; Aldén, M. Experimental apparatus with full optical access for combustion experiments with laminar flames from a single circular nozzle at elevated pressures. *Rev. Sci. Instrum.* **2015**, *86*, 035115.
(51) Hu, S.; Gao, J.; Gong, C.; Zhou, Y.; Bai, X.; Li, Z.; Aldén, M. Assessment of uncertainties of laminar flame speed of premixed flames as determined using a Bunsen burner at varying pressures. *Appl. Energy* **2018**, *227*, 149−158.
(52) Eckbreth, A. *Laser Diagnostics for Combustion Temperature and Species*, 2nd ed.; Gordon and Breach: London, U.K., 1996.
(53) Luque, J.; Crosley, D. R. *LIFBASE: Database and Spectral Simulation (Version 1.5)*; SRI International: Menlo Park, CA, 1999; SRI International Report MP 99-009.
(54) Settersten, T. B.; Patterson, B. D.; Gray, J. A. Temperature- and species-dependent quenching of NO $A^2\Sigma^+(v' = 0)$ probed by two-photon laser-induced fluorescence using a picosecond laser. *J. Chem. Phys.* **2006**, *124*, 234308.
(55) Chang, A. Y.; Dirosa, M. D.; Hanson, R. K. Temperature-Dependence of Collision Broadening and Shift in the NO A ← X (0,0) Band in the Presence of Argon and Nitrogen. *J. Quant. Spectrosc. Radiat. Transfer* **1992**, *47*, 375−390.
(56) Bouvet, N.; Chauveau, C.; Gökalp, I.; Lee, S.-Y.; Santoro, R. Characterization of syngas laminar flames using the Bunsen burner configuration. *Int. J. Hydrogen Energy* **2011**, *36*, 992−1005.
(57) Andrews, G.; Bradley, D. Determination of burning velocities: A critical review. *Combust. Flame* **1972**, *18*, 133−153.
(58) Egolfopoulos, F.; Hansen, N.; Ju, Y.; Kohse-Höinghaus, K.; Law, C.; Qi, F. Advances and challenges in laminar flame experiments and implications for combustion chemistry. *Prog. Energy Combust. Sci.* **2014**, *43*, 36−67.
(59) Clavin, P.; Williams, F. A. Effects of molecular diffusion and of thermal expansion on the structure and dynamics of premixed flames in turbulent flows of large scale and low intensity. *J. Fluid Mech.* **1982**, *116*, 251−282.
(60) Matalon, M.; Matkowsky, B. J. Flames as gasdynamic discontinuities. *J. Fluid Mech.* **1982**, *124*, 239−259.

https://dx.doi.org/10.1021/acs.energyfuels.0c03520
Energy Fuels 2021, 35, 7179−7192

(61) The OpenFOAM Foundation. *OpenFOAM, Version 7*; The OpenFOAM Foundation: London, U.K., 2019; https://openfoam.org.
(62) Goodwin, D. G.; Speth, R. L.; Moffat, H. K.; Weber, B. W. *Cantera: An Object-Oriented Software Toolkit for Chemical Kinetics, Thermodynamics, and Transport Processes, Version 2.4.0*; California Institute of Technology (Caltech): Pasadena, CA, 2018; https://www.cantera.org.
(63) Sutherland, W. LII. The viscosity of gases and molecular force. *London, Edinburgh, and Dublin Philosophical Magazine and Journal of Science* **1893**, *36*, 507−531.
(64) Kee, R. J.; Dixon-Lewis, G.; Warnatz, J.; Coltrin, M. E.; Miller, J. A. *A Fortran Computer Code Package for the Evaluation of Gas-Phase Multicomponent Transport Properties*; Sandia National Laboratories: Livermore, CA, 1986; Technical Report SAND-86-8246.
(65) Zhong, S.; Zhang, F.; Jangi, M.; Bai, X.-S.; Yao, M.; Peng, Z. Structure and propagation of n-heptane/air premixed flame in low temperature ignition regime. *Appl. Energy* **2020**, *275*, 115320.
(66) Zhang, N.; Zhang, F.; Zhong, S.; Peng, Z.; Yu, J.; Liu, H.; Xu, C. Numerical and theoretical investigation of ethanol/air flame instability. *Combust. Theory Modell.* **2020**, *24*, 1108−1129.
(67) Zhong, S.; Zhang, F.; Peng, Z.; Bai, F.; Du, Q. Roles of CO_2 and H_2O in premixed turbulent oxy-fuel combustion. *Fuel* **2018**, *234*, 1044−1054.
(68) Zhong, S.; Zhang, F.; Du, Q.; Peng, Z. Characteristics of reactivity controlled combustion with *n*-heptane low temperature reforming products. *Fuel* **2020**, *275*, 117980.
(69) Duynslaegher, C.; Jeanmart, H.; Vandooren, J. Ammonia combustion at elevated pressure and temperature conditions. *Fuel* **2010**, *89*, 3540−3545.

https://dx.doi.org/10.1021/acs.energyfuels.0c03520
Energy Fuels 2021, 35, 7179−7192